

Comparison of Hydrothermally-grown vs Electrodeposited Cobalt Sulfide Nanostructures as Modified Electrodes for Oxygen Evolution and Electrochemical Sensing Applications

Xinyu Li^{1,#}, Surbhi Sharma^{1,#}, Damien W. M. Arrigan,¹ and Debbie S. Silvester^{1,*}

¹*School of Molecular and Life Sciences, Curtin University, GPO Box U1987, Perth, WA 6845, Australia.*

[#] *These authors contributed equally.*

^{*} *Corresponding author: d.silvester-dean@curtin.edu.au*

Abstract

A wide range of electrocatalysts have been developed and implemented for electrochemical applications over the last decades, with researchers typically using either a conventional synthesis method (followed by drop-casting or spray-coating onto the electrode), or directly electrodepositing the catalyst. However, a clear comparison of the different materials synthesis techniques, and how this affects the electrochemical applications, has been less explored. Herein, we report a direct comparison of fabricated cobalt sulfide (CoS) nanostructure-based electrodes prepared by two different methods for two applications: (a) electrochemical water splitting and (b) glucose sensing. CoS is grown in the form of nanoflowers and nanosheets *via* facile one-pot hydrothermal (HT) and electrodeposition (ED) methods, respectively. Characterization is performed using X-ray diffraction (XRD), scanning electron microscopy (SEM), energy dispersive X-ray spectroscopy (EDX), and X-ray photoelectron spectroscopy (XPS). It is observed that the as-fabricated CoS-ED electrode demonstrated enhanced oxygen evolution reaction (OER) performance, a lower overpotential (~ 166 mV at 10 mA cm⁻²), lower charge transfer resistance (~ 372 Ω), a lower Tafel slope (86 mV dec⁻¹), and better stability compared to the CoS-HT electrode. Moreover, the CoS-ED electrode-based sensor also exhibited better performance, higher sensitivity, better selectivity, and good stability for electrochemical glucose detection in comparison to the CoS-HT sensor.

Keywords

Cobalt sulfide, electrodeposition, hydrothermal synthesis, oxygen evolution reaction, glucose sensing

Introduction

The depletion of fossil fuels and increased environmental concerns have triggered an urgent demand for exploring clean and sustainable alternative energy resources to meet future energy needs.^{1, 2} Electrochemical water splitting has been established as a green and sustainable technology for hydrogen (H₂) production, and is being investigated to help solve the energy crisis. Also, the exploration and development of highly sensitive and fast electrochemical sensors for analytes such as glucose sensing is highly desirable because of the wide variety of applications in different areas such as the food industry, clinical diagnostics, industrial research, and life science.³⁻⁷ Various electrocatalyst-modified electrodes have been widely studied by researchers for both electrochemical water splitting and electrochemical sensing applications.^{1, 3, 5, 7-17}

The oxygen evolution reaction (OER) – one half of the electrochemical water splitting process – is a sluggish process due to the involvement of four electrons. State-of-the-art IrO₂ and RuO₂ materials are recognized as benchmark electrocatalysts for the OER owing to their low onset potentials to trigger the reaction. However, large-scale applications using these materials are greatly limited by their high cost and low reserves. Over the past few years, extensive efforts have been devoted to develop highly efficient and earth-abundant electrocatalysts for the OER, including those based on transition metal oxides^{18, 19}, transition metal sulfides²⁰⁻²³, and transition metal phosphides²⁴⁻²⁶.

Various synthesis methods and different morphologies of electrocatalyst materials have been investigated, however, poor chemical stability, non-homogenous coverage, low efficiency, and high cost are still major limitations. Similar concerns have also been raised when utilizing nanomaterial-modified electrodes for electrochemical glucose sensing.^{3, 6, 13, 15, 27, 28} Therefore, the selection and development of electrocatalyst materials with high activity, good stability, and low cost are of great importance for achieving efficient water splitting and glucose sensing.

Owing to the unique electrical, optical, and magnetic properties of cobalt sulfide (CoS), this material is considered to be a potential candidate for various applications including

photocatalysis, supercapacitors, and solar cells.²⁹⁻³³ In recent years, CoS has been synthesized by different methods and used for electrochemical water splitting³⁴⁻³⁶ as well as electrochemical sensing applications.^{4, 6, 28, 37} On the one hand, deposition of the CoS material directly onto different electrode substrates, such as fluorine doped tin oxide (FTO), indium doped tin oxide (ITO), Ni foam, and glassy carbon (GC) electrodes through the electrodeposition process has been widely reported in the literature.^{4, 31, 33-36, 38, 39} On the other hand, CoS electrocatalyst materials in various morphologies such as nanorods, nanoparticles, and nanoflowers have been synthesized using facile hydrothermal methods.^{6, 32, 37}

Hydrothermal (HT) synthesis is a relatively simple conventional technique for preparing nanomaterials in various morphologies under high pressure and temperature conditions¹⁹⁻²³. Typically, fabrication of electrodes using the hydrothermal method is a two-step procedure involving: (i) synthesis of the electrocatalyst in its powder form, and (ii) preparation of nanostructured films on conducting electrode substrates. In contrast, electrodeposition (ED) processes occur when a film of the electrocatalyst is grown directly on a conducting substrate by performing either cyclic voltammetry^{30, 31, 36, 38, 39} or chronoamperometry⁴⁰ in an electrochemical cell containing the required precursors. In the hydrothermal method, by changing the reaction conditions such as reaction time, temperature, solvents, molar ratio of precursors, and types of ligands, the preparation of a wide range of morphologies of nanomaterials and their further modification is feasible. However, the fabrication of electrodes then becomes a time-consuming and cumbersome process, often with requirements of binders and epoxy resin for good adhesion to the conducting substrates. It is noteworthy that the Nafion is widely used as a binder for the preparation of electrode films by spray coating and drop casting method to enable good adhesion, but it also blocks the active sites leading to a reduction in the activity of the catalyst.⁴¹

Alternatively, the preparation of nanostructured films by electrodeposition is a relatively fast process with many advantages, such as being binder free, having good stability, cost effectiveness, and being environmentally friendly.^{4, 31, 33-35} Despite its many advantages,

the electrodeposition method is restricted to only certain compounds and morphologies of nanomaterials, and further processing of the materials, such as forming nanocomposites, substitution, or doping etc. is more difficult. It can therefore be concluded that both techniques have their advantages and disadvantages, depending on the requirements of the application. It is therefore of great importance to compare the conventionally used hydrothermal method with the electrodeposition method to shed light on future research into the best method to modify electrodes. To the best of our knowledge, a detailed systematic comparison between fabricated nanostructured electrodes by hydrothermal and electrodeposition methods for two different applications has not yet been reported in the literature.

In this work, the CoS electrodes (CoS-HT and CoS-ED) have been successfully fabricated by both hydrothermal (HT) and electrodeposition (ED) methods for their effective utilization in dual electrochemical applications towards the OER and for glucose detection. The CoS-HT electrode has been fabricated in two steps: (i) growth of CoS nanoflowers by a facile hydrothermal method, followed by (ii) preparation of the nanostructured film on a conducting FTO substrate using a spray coating method. Whereas the CoS-ED electrode has been fabricated by film deposition on a fluorine-doped tin oxide (FTO) substrate *via* a single step electrodeposition method. SEM images confirmed the growth of hydrothermally grown and electrodeposited CoS material in the form of nanoflowers and nanosheets, respectively. It is observed that the CoS-ED electrode demonstrates enhanced performance, better intrinsic activity and higher stability compared to the CoS-HT electrode for both OER and glucose detection, and is recommended as the optimum synthesis method for this nanocatalyst.

Experimental

Materials

Cobalt chloride hexahydrate ($\text{CoCl}_2 \cdot 6\text{H}_2\text{O}$), thiourea ($\text{SC}(\text{NH}_2)_2$), nafion 117 ($\text{C}_7\text{HF}_{13}\text{O}_5\text{S} \cdot \text{C}_2\text{F}_4$), and isopropanol ($\text{C}_3\text{H}_8\text{O}$) were purchased from Sigma-Aldrich (Castle Hill, NSW, Australia). Potassium hydroxide (KOH) and glucose were purchased from Ajax Finechem (Taren Point, NSW, Australia). All other analytes such as lactose ($\text{C}_{12}\text{H}_{22}\text{O}_{11}$), fructose ($\text{C}_6\text{H}_{12}\text{O}_6$), ascorbic acid ($\text{C}_6\text{H}_8\text{O}_6$), dopamine ($\text{C}_8\text{H}_{11}\text{NO}_2$), urea ($\text{CH}_4\text{N}_2\text{O}$), sodium chloride (NaCl), and fluorine-doped tin oxide (FTO) glass substrates were purchased from Sigma-Aldrich, Australia. All analytical grade reagents were used without any further modification. Ultrapure water was used as a solvent in all the electrochemical experiments.

Hydrothermal preparation of CoS nanoflowers

CoS nanoflowers were successfully prepared by a facile hydrothermal method reported previously.^{23,42} In a typical procedure, 2 g of $\text{CoCl}_2 \cdot 6\text{H}_2\text{O}$ was dispersed in 30 mL of deionized (DI) water and magnetically stirred for 30 min at room temperature. Afterwards, 0.65 g of $\text{SC}(\text{NH}_2)_2$ was added into the above solution and vigorously stirred for another 30 min. The solution was then transferred into a 50 mL capacity Teflon-lined stainless-steel autoclave and heated to 170 °C for 12 h. After naturally cooling down to room temperature, the resultant black powder was collected by filtration and washed several times with ultrapure water and ethanol. Finally, the sample was dried at 60 °C for 24 h. The obtained powdered sample is denoted by CoS-HT and employed in the fabrication of electrodes without any post treatment.

Preparation of CoS-HT Film

Typically, 10 mg of the synthesized catalyst was dispersed in 10 mL of isopropanol and ultrasonicated for 30 min followed by stirring for 2 h to prepare a homogenous solution. Afterwards, 50 μL nafion 117 solution (5 wt.%) was dropwise added into above solution under stirring. The catalyst solution was spray-coated on the FTO ($\sim 1.5 \text{ cm}^2$) substrate using a spray gun (Ozito, 150 W) with a nitrogen flow, followed by drying at 80 °C for 2 h. The spray

deposited CoS-HT film on the FTO substrate was carefully covered with epoxy resin and utilized for the fabrication of the nanostructured electrodes.

Electrodeposition of CoS film

Electrodeposition of the CoS film was performed on a PGSTAT101 Autolab potentiostat (Eco, Chemie, Netherlands) interfaced to a PC with Nova 1.11.2 software, at room temperature inside an aluminum Faraday cage. For deposition of the CoS film, a conventional three-electrode cell assembly using a FTO glass substrate ($\sim 1.5 \text{ cm}^2$) as the working electrode, graphite rod as the counter electrode, and Ag/AgCl (4 M KCl, Pine Research Instrumentation, Durham, NC, USA) as the reference electrode was employed. In a typical electrodeposition experiment, 0.06 g of $\text{CoCl}_2 \cdot 6\text{H}_2\text{O}$ was first dissolved in 50 mL ultrapure water and afterwards, 1.9 g of $\text{SC}(\text{NH}_2)_2$ was added into the above solution under vigorous stirring for 30 min at room temperature. Electrodeposition of the CoS film was performed using cyclic voltammetry (CV) within a potential range of -1.2 to $0.2 \text{ V vs. Ag/AgCl}$ (starting initially at 0 V and scanning positively) at a scan rate of 5 mVs^{-1} for 15 scan cycles³⁶. The as-deposited CoS/FTO film was rinsed with ultrapure water and ethanol and dried at $80 \text{ }^\circ\text{C}$ for 2 h. The electrodeposited film on the FTO substrate is denoted by CoS-ED. A schematic diagram for the formation of the CoS-HT powder, CoS-HT film, and CoS-ED film is illustrated in Figure 1.

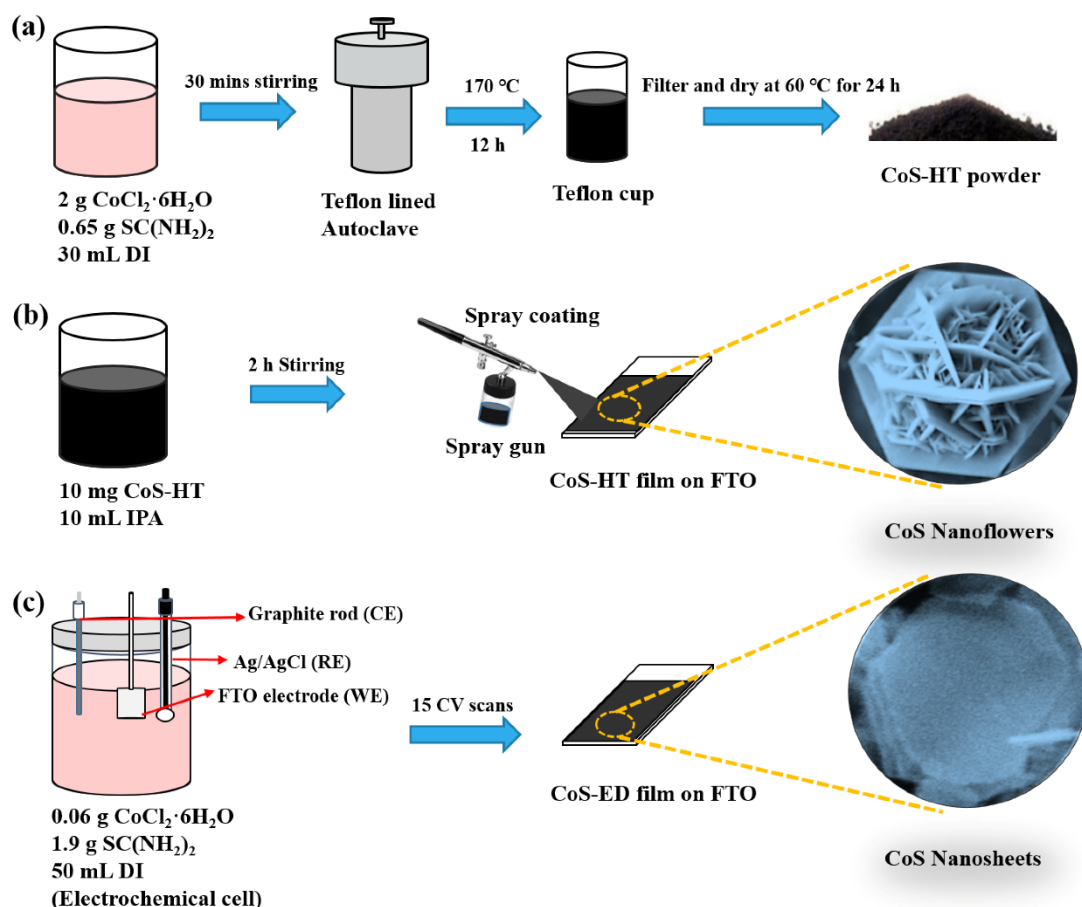
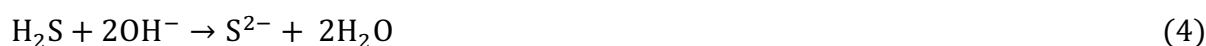


Figure 1. Schematic illustration of (a) hydrothermal synthesis of CoS-HT powder, (b) deposition of CoS-HT film on FTO substrate by spray coating method, and (c) deposition of CoS-ED on FTO substrate using the electrodeposition method.

Synthesis method of CoS-HT nanoflowers

For the synthesis of CoS-HT, cobalt chloride ($\text{CoCl}_2 \cdot 6\text{H}_2\text{O}$) – which acts as a source of cobalt – and thiourea ($\text{SC}(\text{NH}_2)_2$) – which serves as a sulfur source, as well as a structure directing agent – were used as the precursors. The method for the synthesis of CoS in a nanoflower-like morphology involves the following steps: (i) growth of CoS in the form of nanosheets and their eventual growth into CoS nanosphere-like structure; (ii) conversion of smaller CoS nanoflakes into larger nanoflakes through the process of Ostwald ripening to form a nanosphere like structure, and finally (iii) the formation of CoS nanoflowers *via* the process of dissolution-recrystallization.^{23, 42} ($\text{SC}(\text{NH}_2)_2$) becomes hydrolyzed to form hydrogen sulfide (H_2S), ammonia (NH_3) and carbon dioxide (CO_2). Then, the formed cobalt cations (Co^{2+}) react with NH_3 to form a $[\text{Co}(\text{NH}_3)_4]^{2+}$ complex. Furthermore, the formed NH_3 becomes hydrolyzed,

which further results in the formation of S^{2-} anions. Finally, the formed $[Co(NH_3)_4]^{2+}$ cations react with S^{2-} anions, leading to the formation of nanoflower-like CoS nanostructures denoted by CoS-HT. The formation mechanism of the CoS-HT nanoflowers can be described by the following reactions (eqs. 1-5):^{23, 42}



It is noteworthy that the hierarchical nanoflower-like structure of CoS would be beneficial in providing a larger number of interfacial sites for both the OER and electrochemical glucose sensing reactions.

Synthesis method of CoS-ED nanosheets

Cyclic voltammetry was applied for the electrodeposition of CoS film on the FTO substrate (see Figure S1, supplementary material). Briefly, 5 mM of $CoCl_2 \cdot 6H_2O$ and 0.5 M of thiourea (TU) precursors were used to prepare 50 mL of solution. The as-prepared solution was transferred to the electrodeposition cell and CV scans ranging from 0 to +0.2 V down to -1.2 V and back to 0 V were applied for 15 cycles using a three-electrode assembly. The possible reactions involved in the electrodeposition of CoS-ED film have been suggested as follows (eq. 6 and 7):^{30, 31}



During the anodic sweep from 0 to 0.2 V, thiourea (TU) reacts with cobalt cations (Co^{2+}) to form the complex ($Co(TU)_2^{2+}$). During the cathodic sweep, reduction of the formed complex leads to the formation of CoS. The peak at approximately -0.6 V is ascribed to the reduction

of $\text{Co}(\text{TU})_2^{2+}$ to CoS. Thus, with an increasing number of CV scans, CoS is electrodeposited on the conducting side of the FTO substrate.

Electrochemical water splitting and sensing measurements

Electrochemical water splitting and electrochemical sensing experiments were conducted using a PGSTAT101 Autolab potentiostat (Eco, Chemie, Netherlands) interfaced to a PC with Nova 1.11.2 software. Electrochemical impedance spectroscopy (EIS) tests were conducted using a PalmSens4 potentiostat (PalmSens, Houten, the Netherlands), interfaced to PC with PSTrace 5.8 software. All the electrochemical water splitting and electrochemical sensing experiments were performed at room temperature inside an aluminum Faraday cage. All electrochemical measurements were performed in a typical three-electrode setup with an electrolyte solution of 1 M KOH, using fabricated CoS electrodes as the working electrode, a graphite rod as counter electrode, and Hg/HgO (1 M KOH (pH=14), BASi, USA) as a reference electrode. Linear sweep voltammetry (LSV) measurements were conducted at a scan rate of 5 mVs^{-1} within a potential range of -0.2 to 0.8 V vs. Hg/HgO . The EIS test was carried out by applying a 10 mV AC voltage vs. Hg/HgO at open circuit potential in a frequency range from 100 kHz to 0.01 Hz. Stability tests of both samples for the OER were conducted using 100 CV cycles scanned from 0.1 to 0.9 V vs. Hg/HgO at a scan rate of 5 mVs^{-1} . The stability of the catalyst samples was analyzed using chronoamperometry measurements for 20 h continuously in a 1 M KOH solution. All electrochemical measurements were iR corrected and converted to potentials vs. the reversible hydrogen electrode (RHE) using the Nernst equation: $E_{\text{RHE}} = E_{\text{Hg/HgO}} + 0.05916 \text{ pH} + E^0_{\text{Hg/HgO}}$, where E_{RHE} is the potential converted vs. RHE, $E_{\text{Hg/HgO}}$ is the measured potential vs. Hg/HgO reference, and $E^0_{\text{Hg/HgO}} = 0.098 \text{ V}$.

Electrochemical sensing experiments were conducted in a typical three-electrode cell with 0.1M KOH electrolyte solution, using the fabricated CoS electrode as the working electrode, a Pt coil as the counter electrode, and Ag/AgCl (4M KCl, Pine, USA) as the reference.

Characterization

X-ray diffraction (XRD) patterns were recorded in a 2θ range of $20\text{--}80^\circ$ on a diffractometer (D8 Advance Bruker AXS) using $\text{CuK}\alpha$ radiation ($\lambda = 1.5418 \text{ nm}$). Scanning electron microscopy (SEM) as well as energy dispersive X-ray spectroscopy (EDX) were performed using FIBSEM (Zeiss NEON 40 EsB CrossBeam) for morphological and elemental composition analysis of the samples. X-ray photoelectron spectroscopy (XPS) was conducted using a spectrometer (Kratos AXIS Ultra DLD) under an ultrahigh vacuum atmosphere (1×10^{-9} mbar) for investigating the chemical composition and oxidation states of the elements. All elements were calibrated by setting the dominant C 1s peak at 284.5 eV. The measurements were carried out under a charge neutralizer to overcome charging of the sample.

Results and discussion

Characterisation of the CoS prepared materials and films

The crystalline structure and phase purity of the hydrothermally grown CoS powdered sample and electrodeposited CoS film were investigated by XRD analysis. Figure 2a shows XRD patterns of the as-prepared hydrothermal CoS nanostructures which reveals the formation of a hexagonal structure of CoS well matched with the standard diffraction patterns of CoS (JCPDF file No. 01-075-0605). No impurity peaks were observed, which clearly confirms the synthesis of a highly crystalline CoS-HT sample. Figure 2b shows the XRD pattern of the as-prepared CoS-ED film compared to the bare FTO substrate. It is noted that the peaks of the CoS-ED film are similar to that observed for bare FTO indicating the amorphous nature of the electrodeposited film, which is consistent with a previous report.³⁶

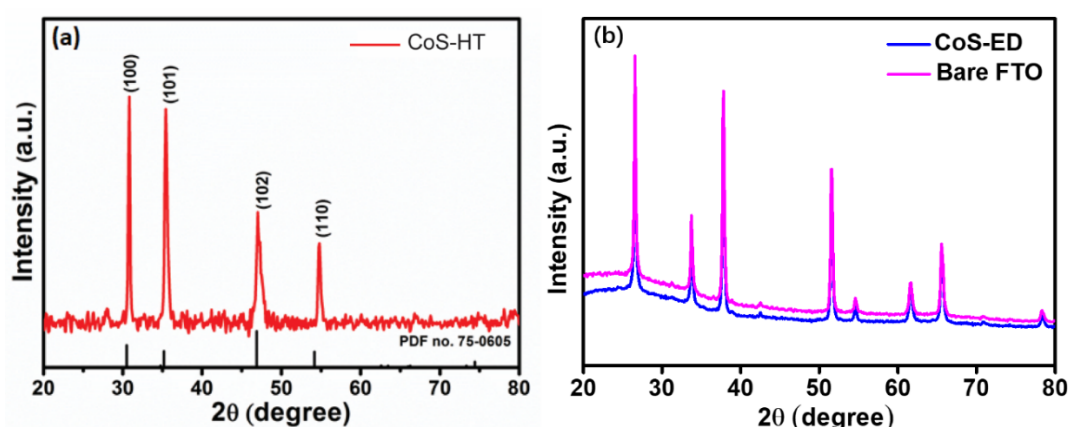


Figure 2. X-ray diffraction patterns of the as-prepared (a) CoS-HT sample; black lines represent the standard JCPDF data (card no. 75-0605), and (b) CoS-ED film and bare FTO substrate.

The morphology of the nanostructured samples was analyzed by SEM. Figure 3 shows SEM images of the hydrothermally grown and electrodeposited CoS nanostructures. It is observed from the SEM images that CoS-HT was grown in the form of three-dimensional (3D) flower-like structure with interconnected nanosheets with length of a few microns, as illustrated in Figures 3a and 3b. SEM images of the as-deposited CoS-ED film on the FTO substrate confirmed the growth of CoS in the form of nanosheets, as shown in Figures 3c and 3d.

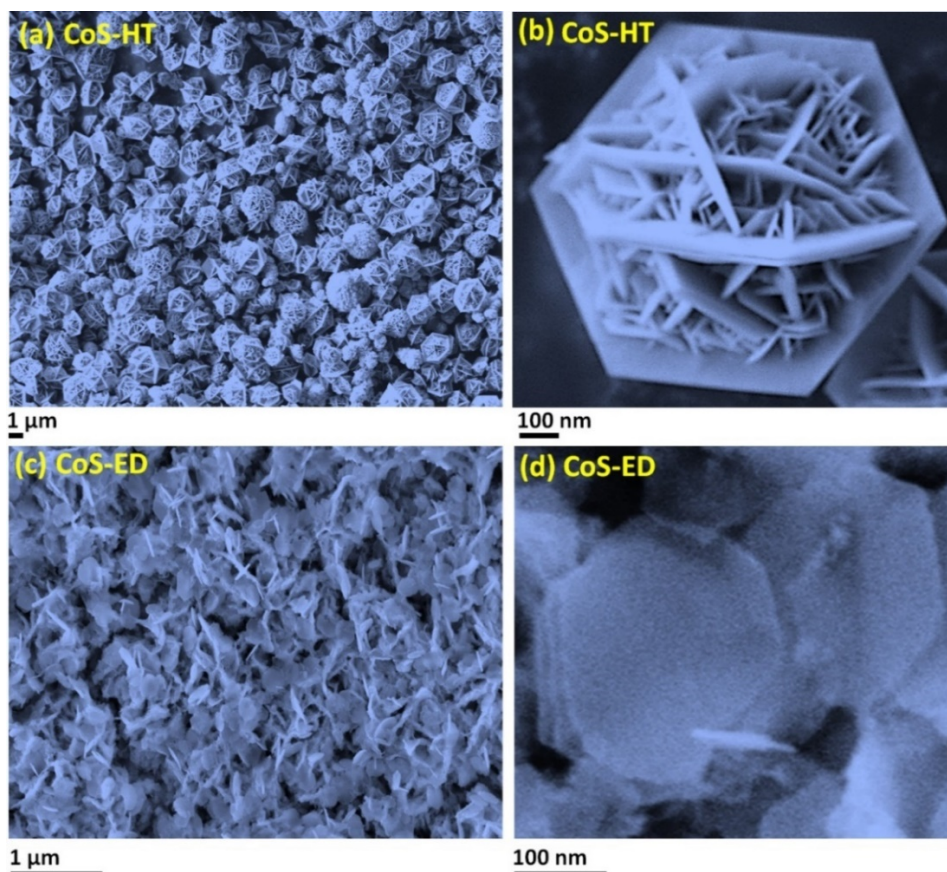


Figure 3. SEM images of (a,b) CoS-HT nanoflowers synthesized by hydrothermal method, and (c,d) as-deposited CoS-ED film by electrodeposition method.

To investigate the elemental composition and corresponding mapping of the CoS nanostructures, EDX analysis was performed. EDX of the powdered CoS-HT sample confirmed the formation of CoS nanoflowers in an atomic ratio of 1:1 (see Figure S2). Figure 4 shows a SEM image of the CoS-HT and CoS-ED films with the elemental mapping and corresponding EDX spectrum. It reveals that the constituent elements of cobalt (Co), and sulfur (S) are present in the as-deposited CoS-HT film, and are distributed uniformly on the FTO substrate (Figure 4a). The spatial distribution of the constituent element Co is found to be well matched with the spatial distribution of S present in the CoS-HT film on the FTO substrate, as shown in Figure 4b and 4c. It should be noted that fluorine (F), tin (Sn), silicon (Si), and oxygen (O) are the constituent elements found in the FTO substrate. Thus, the elemental mapping images and the peaks for Co (39.14%), and S (44.73%) along with F (9.94%), Sn (2.78%), Si (0.21%), and O (3.2%) are identified in the EDX analysis with no other impurity peaks (Figure 4d-g). Furthermore, the CoS-ED film is found to be homogenous and closely packed (Figure 4d-g).

4i). The spatial distribution of the Co and S elements present in the CoS-ED film along with F, Sn, Si, and O due to the FTO substrate is demonstrated by elemental mapping images (Figure 4j-o). Figure 4p illustrates the EDX spectrum of the CoS-ED film confirming the presence of constituent elements Co (14.38 %), S (14.92%) with other elements F (1.83%), Sn (22.58%), Si (0.68%), and O (45.61%).

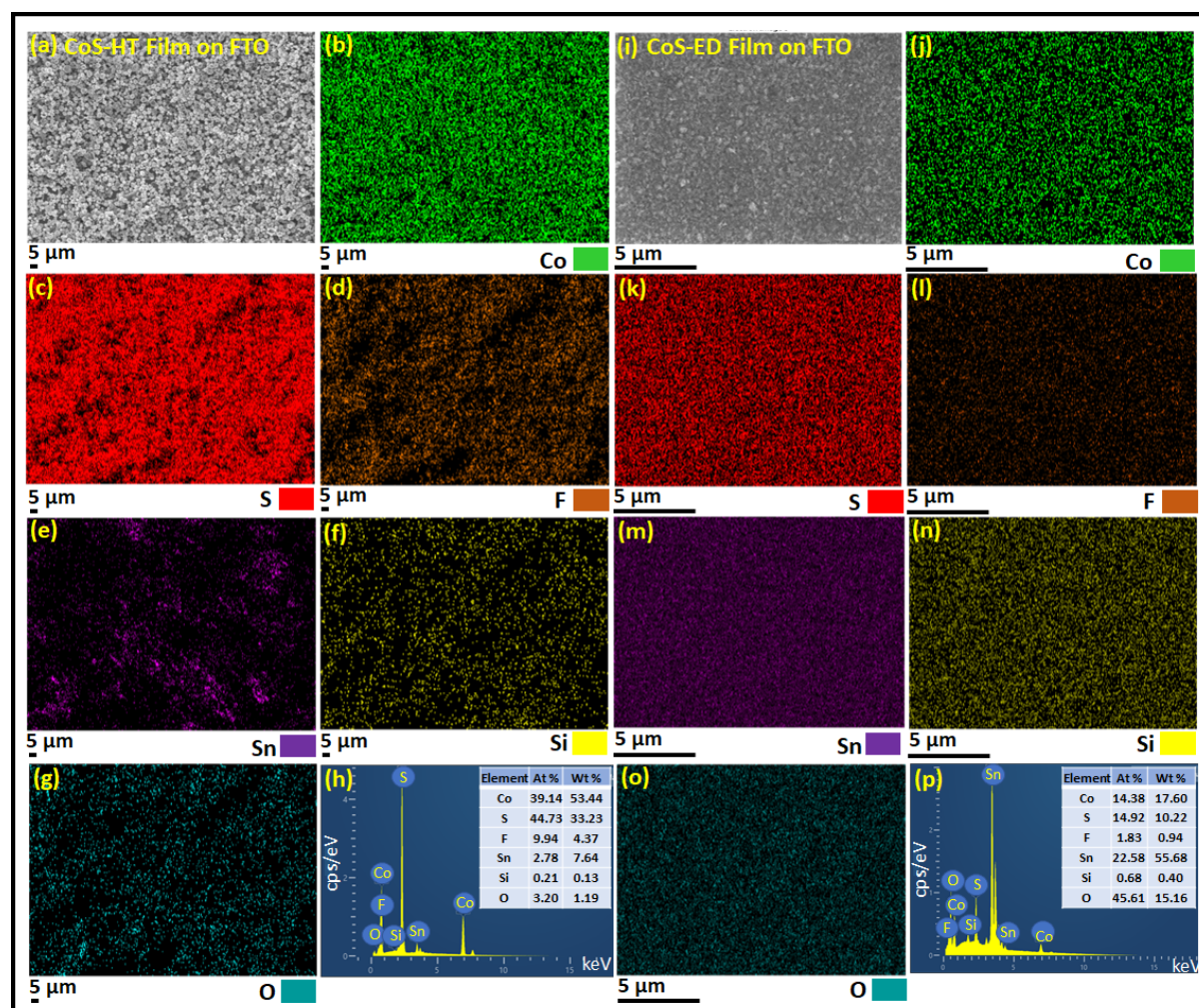


Figure 4. (a) SEM image of CoS-HT and corresponding elemental mapping images of (b) cobalt (green), (c) sulfur (red), (d) fluorine (brown), (e) tin (purple), (f) silicon (yellow), and (g) oxygen (cyan). (h) Respective EDX spectrum, and (i) SEM image of CoS-ED and corresponding elemental mapping images of (j) cobalt (green), (k) sulfur (red), (l) fluorine (brown), (m) tin (purple), (n) silicon (yellow), (o) oxygen (cyan), and (p) the respective EDX spectrum.

To further investigate the valence states of the elements and the chemical composition of the surface of the CoS nanostructures, XPS analysis was carried out. Figure 5 shows the Co 2p and S 2p peaks, and O 1s peaks for CoS-HT and CoS-ED samples, confirming the presence of Co, S, and O in both samples. The Co 2p spectrum of CoS-HT, as shown in Figure 5a, shows

two main peaks at 778.4 and 793.9 eV, corresponding to the Co 2p_{3/2} and Co 2p_{1/2} states, confirming the presence of Co²⁺ in CoS-HT, along with shakeup satellite peaks at 780.3 and 799.4 eV, respectively.^{23, 43}

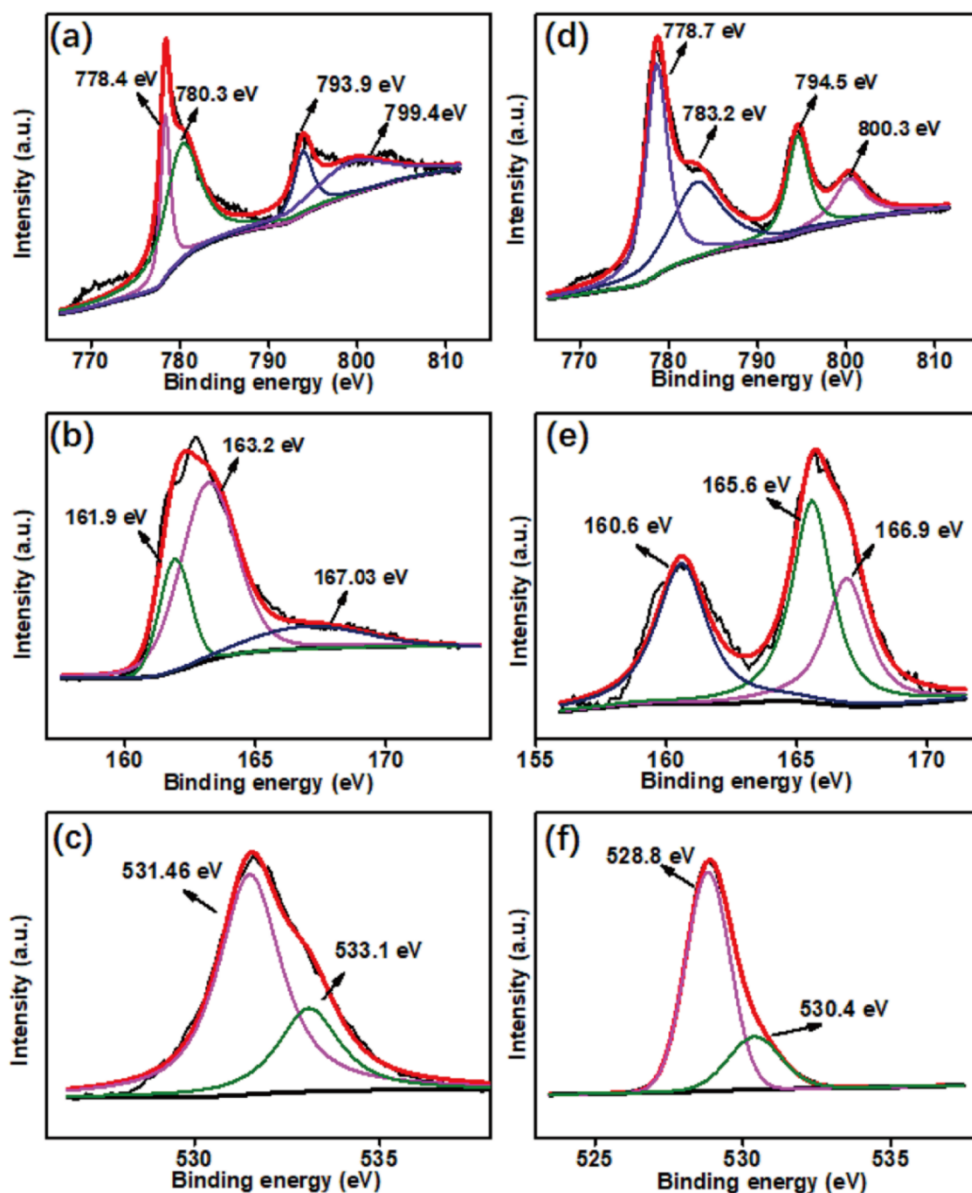


Figure 5. X-ray photoelectron spectroscopy (XPS) patterns of (a,b) Co 2p, (b,e) S 2p and (c,f) O 1s of the as-prepared CoS-HT and CoS-ED samples, respectively.

Figure 5b displays the S 2p spectrum of CoS-HT, with two main peaks at 161.9 and 163.2 eV corresponding to S 2p_{3/2}, and S 2p_{1/2} states, respectively, indicating the presence of S²⁻ in the sample.^{23, 43} Another broad peak with a weak intensity at 167.07 eV is observed, which corresponds to a trace amount of SO₄²⁻ anions which may arise due to exposure with air.⁴³ Furthermore, the O 1s spectra shows two peaks at 531.5 and 533.1 eV, indicating the

presence of O^{2-} species possibly due to the substrate. Figure 5d-f illustrates the existence of Co, S, and O elements in the CoS-ED sample. The Co 2p spectrum as shown in Figure 5d, exhibits two spin-orbit doublets with main peaks at 778.7 and 794.5 eV, which correlates to the Co $2p_{3/2}$ and Co $2p_{1/2}$ states signifying the presence of the Co^{2+} species in CoS-ED.^{34, 39} The two satellite peaks at 783.2 and 800.3 eV are attributed to the ground state of Co^{2+} species.³⁴ Figure 5e illustrates the S 2p spectrum with a peak at 160.6 eV corresponding to S $2p_{3/2}$ indicating the presence of S^{2-} in the deposited film³⁰. The appearance of additional peaks at 165.6 and 166.9 eV in CoS-ED, as shown in Figure 5e, could be ascribed to oxidized sulfur which is well reported in the literature.^{30, 31} The main peaks of O 1s core levels at 528.8 and 530.4 eV as shown in Figure 5f, could be ascribed to the substrate.⁴⁴

Electrocatalytic activity towards the OER

To perform a comparative assessment between hydrothermal and electrodeposition methods, a series of electrochemical water splitting measurements such as LSV, EIS, CV, and chronoamperometry tests were conducted using the CoS-HT and CoS-ED FTO-based electrodes. Figure 6a illustrates the LSV plots of the CoS-HT, CoS-ED, and nafion (with no electrocatalyst) on FTO based electrodes. Note that the LSV plots are iR corrected (Figure 6b) and the measured current has been converted to current density (j) by dividing the current by the geometric area of the electrode. All electrodes showed anodic current density evidencing the occurrence of the OER at the surface of electrode. It is observed that the current density for CoS-ED is higher than that of the CoS-HT electrode, whereas the nafion based electrode exhibited negligible current density within the potential range. The value of the overpotential (η) can be determined by subtracting the thermodynamic potential for water splitting (1.23 V vs. RHE) from the measured potential at $j=10 \text{ mA/cm}^2$. The higher activity of the CoS-ED towards the OER is confirmed by the lower overpotential ($\sim 166 \text{ mV}$) compared to $\sim 256 \text{ mV}$ at $j=10 \text{ mA/cm}^2$ for the CoS-HT electrode, both better than previous reports^{23, 34, 35, 43} as shown in Table 1.

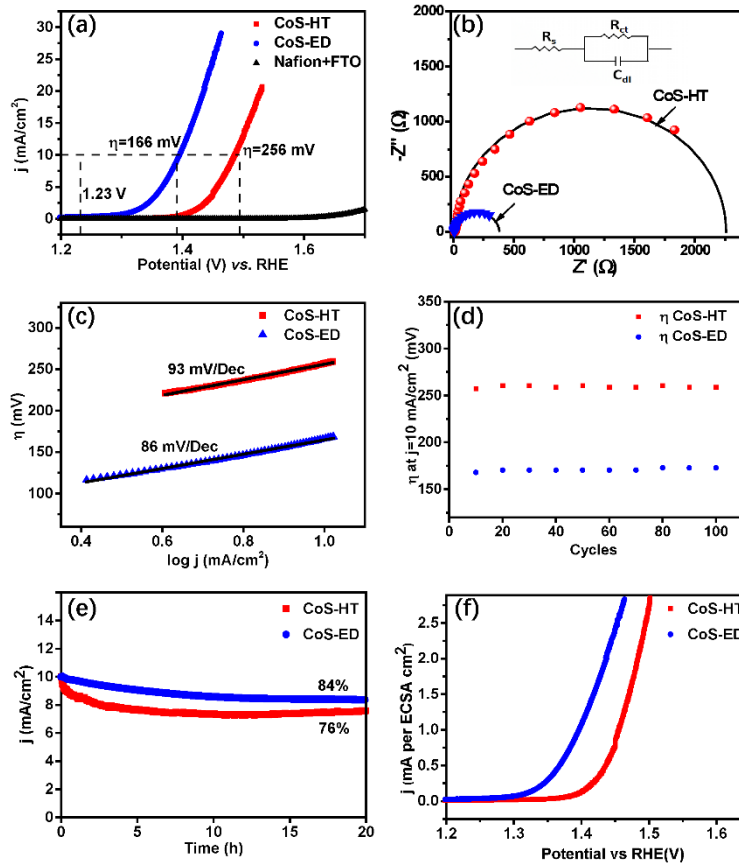


Figure 6. (a) Linear sweep voltammetry (LSV) plots of CoS-HT, CoS-ED, and nafion based electrodes in 1 M KOH solution, (b) EIS-Nyquist plots of CoS-HT and CoS-ED electrodes in 1 M KOH solution; where the points denote the obtained experimental data points and solid line denotes the curve acquired by simulation. Inset of (b) shows the associated equivalent electrical circuit consisting of solution resistance (R_s), charge transfer resistance (R_{ct}), and double layer capacitance (C_{dl}) used for simulation, (c) Tafel plots of CoS-HT, and CoS-ED electrodes, (d) change of overpotential at a current density of 10 mAcm^{-2} for 100 cyclic voltammetry (CV) cycles, and (e) long-term chronoamperometry tests for CoS-HT, and CoS-ED electrodes at a current density of 10 mAcm^{-2} for 20 h. (f) Polarization curves for CoS-HT and CoS-ED, normalized to the ECSA.

Table 1. Comparison of overpotential (η at $j=10 \text{ mA/cm}^2$) for the CoS-based electrodes used in the current work vs previously published reports.

Electrocatalyst	Synthesis method	Substrate	Electrolyte	η (at $j=10 \text{ mA/cm}^2$)	Ref.
CoS Nanosheets	Electrodeposition	Carbon cloth	1 M KOH	390 mV	34
CoS Nanosheets	Electrodeposition	Ti mesh	1 M KOH	361 mV	35
CoS Nanosheets	Electrodeposition	Nickel foam	1 M KOH	297 mV	43
CoS/CNT Nanocomposite	Hydrothermal	GC	1 M KOH	330 mV	23
CoS Nanoflowers	Hydrothermal	FTO	1 M KOH	256 mV	This work
CoS Nanosheets	Electrodeposition	FTO	1 M KOH	166 mV	This work

To investigate the charge transfer kinetics at the electrode/electrolyte interface of the fabricated CoS-HT and CoS-ED electrodes, EIS measurements were performed. Figure 6b

shows the EIS Nyquist plots for CoS-HT and CoS-ED electrodes with the inset showing the equivalent electrical circuit model used for fitting the data. It is noted that the horizontal x-axis of the EIS Nyquist plot denotes the real component (Z') of the impedance, while the vertical y-axis represents the imaginary component (Z''). The acquired experimental data points are fitted into solid lines using the PalmSens software. The equivalent electrical circuit model as shown in the inset to Figure 6b was employed for the simulation of the obtained data points, where R_S is the solution resistance, R_{ct} is the charge transfer resistance, and C_{dl} is the double layer capacitance.⁴⁵ The diameter of the semicircle denotes the value of R_{ct} towards the lower frequency region, while the value of R_S is determined from the intercept near the origin of the semicircle towards the higher frequency region.⁴⁵ The smaller the diameter of the semicircle, the better the charge separation characteristics of the generated charge carriers. It is apparent that the CoS-ED electrode exhibited a much lower R_{ct} value of $372 \pm 0.7 \Omega$ (averaged from three independent tests) as compared to the R_{ct} value of $2253 \pm 1.9 \Omega$ (averaged from three independent tests) for CoS-HT, indicating the faster separation and transfer of the charge carriers at the electrode/electrolyte interface.

Figure 6c shows Tafel plots for the CoS-HT and CoS-ED electrodes. Tafel plots were obtained from the Tafel equation in Eq. 8:^{1, 10, 46}

$$\eta = b \log j + a \quad (8)$$

where η is the overpotential, j is the current density, b is the Tafel slope, and a is a constant. Smaller values of the Tafel slopes are more desirable, as it signifies a higher increase in the current density at lower potentials.^{1, 10, 17, 46} The CoS-HT electrode exhibited a smaller value of the Tafel slope (93 mV/dec) compared to the Tafel slope value of CoS-ED (86 mV/dec), confirming that the CoS-ED electrode demonstrated higher OER activity, which is in agreement with the LSV and EIS results.

Furthermore, good OER performance stability of the fabricated electrodes in the aqueous electrolyte is a bottleneck for real-world water splitting applications. Figure 6d illustrates the change of η at $j=10 \text{ mA/cm}^2$ after 100 cyclic voltammetry (CV) scans for CoS-

HT and CoS-ED electrodes. Both the electrodes demonstrated good stability even after 100 CV cycles. In addition, long-term chronoamperometry measurements were performed over the CoS-HT and CoS-ED electrodes for continuous 20 h (Figure 6e).

To further determine the intrinsic activity of both electrodes, an estimation of the electrochemically active surface area (ECSA) was carried out to normalize the LSV data. CV measurements were conducted in the non-Faradic region at different scan rates (10, 20, 40, 60, 80, 100, and 120 mV s^{-1}) (see Figures S3a and S3b) to estimate the double-layer capacitance (C_{dl}), which is linearly proportional to the ECSA⁴⁷⁻⁵². Figure S3c shows the plots of the difference in current density ($\Delta j/2 = (j_{\text{anodic}} - j_{\text{cathodic}})/2$ at 0.63 V vs. RHE) against the scan rate. The CoS-ED electrode possesses a higher C_{dl} value of 0.41 mFcm^{-2} compared to 0.19 mFcm^{-2} for the CoS-HT electrode. The ECSA is estimated to be 15.3 cm^2 and 7.12 cm^2 for the CoS-ED and CoS-HT electrodes, respectively. The current density shown in Figure 6a is normalized by the ECSA, and the resulting plot is shown in Figure 6f. After normalization, the CoS-ED still shows a better activity towards the OER, indicating that CoS-ED is intrinsically more active than the CoS-HT electrode.

The CoS-ED electrode maintained ~84% of its initial current density even after a long time of 20 h, which is higher compared to ~76% for the CoS-HT electrode. It can be concluded that the CoS-ED electrode demonstrated both better OER activity and stability than the CoS-HT electrode. In addition, EDX measurements of the CoS-HT and CoS-ED electrodes were performed after conducting stability tests (see Figure S4). The stoichiometry of the Co and S elements was almost maintained even after utilization for 20 h, although the Co and S atomic ratio in the film also dropped, which can be ascribed to the formation of CoOOH and the oxidation of S^{2-} to sulphate (that dissolves in the electrolyte) after harsh OER conditions, as reported previously.^{35, 53, 54}

Electrochemical glucose sensing

The as-fabricated CoS-ED and CoS-HT electrodes were also evaluated for glucose sensing applications in 0.1 M KOH electrolyte solution. A scan rate study was conducted at different scan rates from 2 mVs⁻¹ to 200 mVs⁻¹ in the presence of 2 mM glucose (0.1 M KOH as electrolyte), as illustrated in Figures 7a and 7b. It is observed that with increasing scan rate, the current due to the redox reactions increased for both CoS-HT and CoS-ED electrodes. With increasing scan rates, a trend of shifting of the anodic response to a more positive value and the cathodic peak to a more negative value has been observed. Especially, the CoS-ED electrode demonstrated much more distortion of the peaks compared to CoS-HT indicating a more capacitive nature of the material. Both anodic and cathodic peak currents (I_p) vary linearly with respect to the square root of the scan rates between 2 to 200 mVs⁻¹, as shown in the insets of Figures 7a and 7b. However, both the plots showed a non-zero intercept, suggesting that the redox reaction is a mixed adsorption-diffusion controlled electrochemical process.^{55, 56} The scan rate study for CoS-HT and CoS-ED in the absence of glucose also signifies the occurrence of an adsorption-diffusion controlled mixed electrochemical process (see Figure S5).

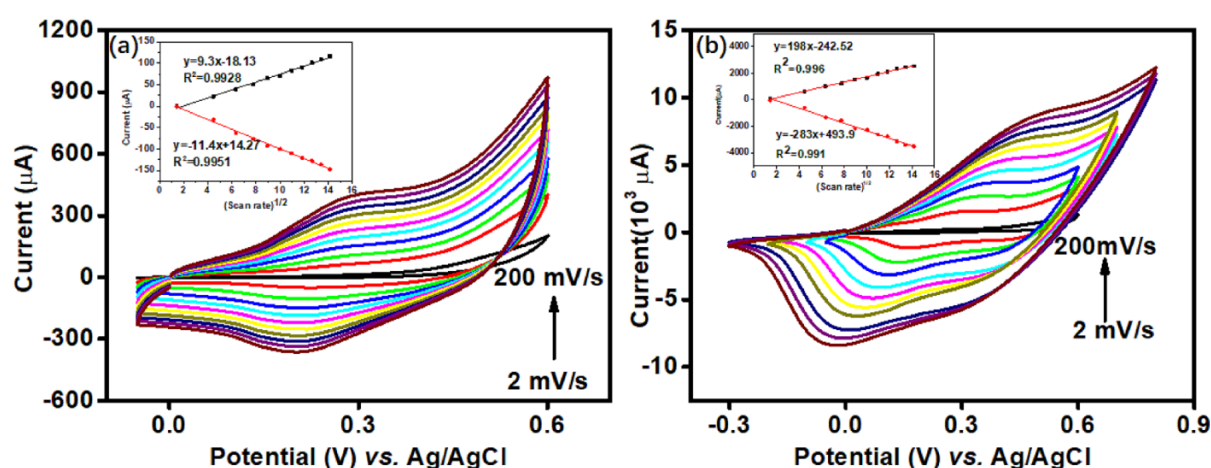


Figure 7. CV curves of the (a) CoS-HT electrode and (b) CoS-ED electrode at different scan rates (2, 20, 40, 60, 80, 100, 120, 140, 160, 180, and 200 mVs⁻¹) in 0.1 M KOH and 2 mM glucose solution. Inset of (a) and (b) show the plots of corresponding peak current versus square root of scan rates.

To investigate the electrochemical sensing mechanism for the CoS modified electrodes, electrochemical responses for different concentrations of glucose ranging from 0 to 10 mM

were measured in 0.1 M KOH under continuous stirring. Figures 8a and 8b illustrate the CV plots of CoS-HT and CoS-ED electrodes with 0-10 mM glucose in 0.1 M KOH, respectively. In the absence of glucose, oxidation peaks are observed at 0.3 and 0.25 V, while the reduction peaks are found at 0.23 and 0.13 V for CoS-HT and CoS-ED electrodes, respectively. The first pair of redox peaks are attributed to the reversible transformation of CoS to CoSOH ($\text{Co}^{\text{II}} \rightleftharpoons \text{Co}^{\text{III}}$) according to the following reaction:^{6,28}



The second redox process is ascribed to the reversible conversion of CoSOH to CoSO ($\text{Co}^{\text{III}} \rightleftharpoons \text{Co}^{\text{IV}}$), as per the following reaction:^{6,28}

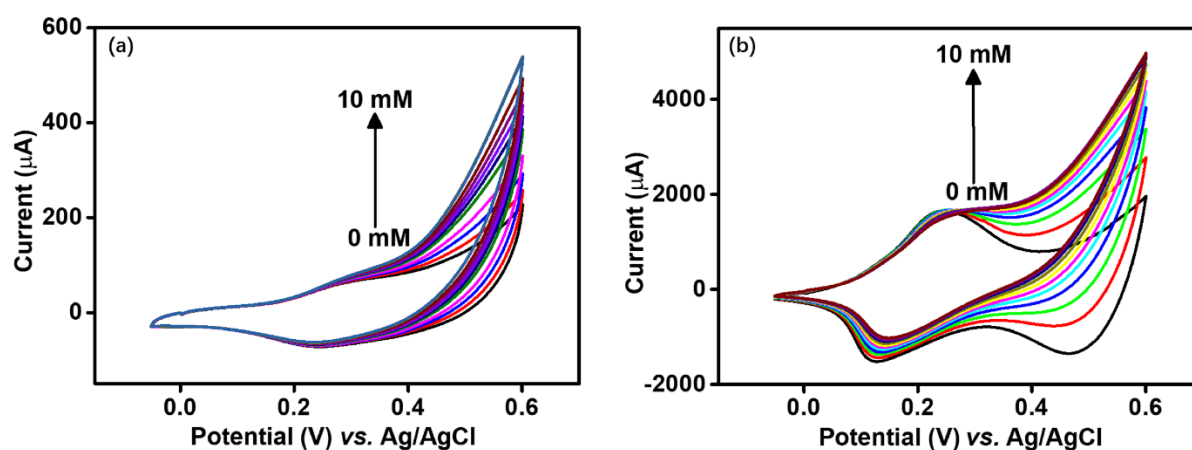
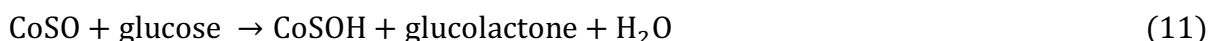


Figure 8. CV curves of the (a) CoS-HT electrode, and (b) CoS-ED electrode without and with different glucose concentration (1-10 mM) at a scan rate of 20 mVs⁻¹.

It is evident that the OH^- ions in the electrolyte play a crucial role in triggering the electrochemical redox reactions. The oxidation of glucose to gluconolactone takes place by the conversion of Co^{IV} to Co^{III} according to the following reaction:⁶



In both electrodes, the cathodic current at 0.5 V decreases with increasing glucose concentration, which is attributed to the consumption of $\text{Co}^{\text{III}}/\text{Co}^{\text{IV}}$ during the conversion of glucose into gluconolactone. Whereas the anodic current at 0.6 V increases prominently with an increase in the glucose concentration due to the oxidation of CoSOH (eq. 10) indicating the

good electrocatalytic activity of CoS for glucose oxidation. Shifting of the anodic peak current is observed possibly due to the change of the pH of the solution due to the formation of glucolactone.

The development of a sensitive sensor is essential for timely monitoring low concentration of glucose. Chronoamperometry tests were therefore performed for both CoS-HT and CoS-ED electrodes using an applied potential of 0.5 V and adding glucose successively under continuous stirring, as depicted in Figure 9a and 9b. Different glucose concentrations of 40 μM , 80 μM , 0.1–1mM (with increments of 0.1 mM), and 2–10 mM (with increments of 1 mM) were employed. The current-time plots showed consecutive step changes of the current on changing glucose concentration at a working potential of 0.5 V in the 0.1 M KOH (Figures 9a and 9b). The leveling off in the current step is observed at high glucose concentrations in both CoS electrodes, possibly due to the occupancy of the surface sites of the electrodes with glucose molecules thus affecting the diffusion of glucose molecules towards the electrode surface⁵⁷⁻⁵⁹. Alternatively, it may exhibit Michaelis-Menten kinetics, similar to an enzyme behaviour, so levelling off could be expected.

The insets of Figures 9a and 9b depict the calibration curves for both electrodes with a linear fitting in the low and high concentration regions (where error bars denote the standard deviations over three runs on freshly prepared electrodes). For the CoS-HT electrode, a linear current response began at 0.2 mM which continued until 2 mM glucose concentration, followed by a second linear region from 3 mM to 10 mM glucose. Similarly, for CoS-ED electrode, the first linear current response started at 80 μM which continued until 1 mM, followed by a second linear region from 2 to 10 mM glucose. The sensitivity of the CoS-HT sensor is estimated as $\sim 13.8 \mu\text{AmM}^{-1}\text{cm}^{-2}$ in the lower concentration range (0.2-2 mM) and $\sim 6.64 \mu\text{AmM}^{-1}\text{cm}^{-2}$ in the higher concentration range (3-10 mM). It is evident that the CoS-ED sensor is far more sensitive than the CoS-HT sensor with a sensitivity of $\sim 330.13 \mu\text{AmM}^{-1}\text{cm}^{-2}$ and $\sim 55.53 \mu\text{AmM}^{-1}\text{cm}^{-2}$ in the lower concentration range (80 μM –1mM) and higher concentration range

(2–10 mM), respectively. The improved sensitivity of the CoS-ED electrode is partially attributed to the higher ECSA of CoS-ED compared to that of CoS-HT, which facilitates more active sites for the detection of the glucose.

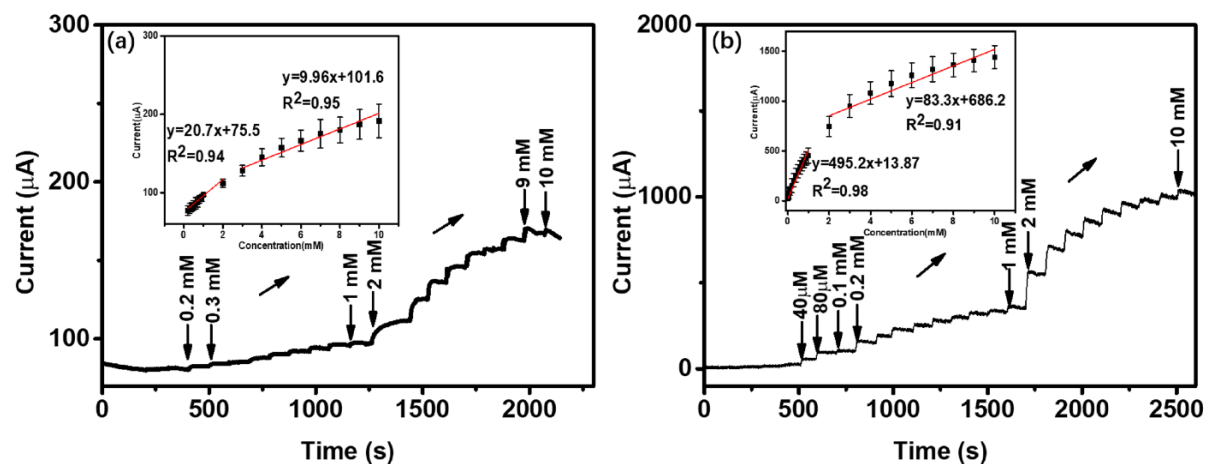


Figure 9. Chronoamperometry response of (a) CoS-HT and (b) CoS-ED electrode with different concentration of glucose in 100 mL of 0.1 M KOH solution with continuous stirring. Inset of (a) and (b) show the corresponding calibration curves for current response versus glucose concentration (error bars denote the standard deviations for three repeat runs on freshly prepared electrodes).

Selectivity is a crucial factor for analyzing the performance of electrochemical glucose sensors.^{6, 28} Therefore, selectivity tests for CoS-HT and CoS-ED sensors in the presence of various interfering analytes such as lactose, fructose, ascorbic acid (AA), dopamine (DA), urea, and sodium chloride (NaCl) were conducted, as shown in Figures 10a and 10b. The selectivity experiments were performed by the addition of 1 mM glucose and addition of 1 mM of each interferent successively in 0.1 M KOH under continuous stirring. It is observed that with the addition of 1 mM of glucose, the current increased significantly, while no noticeable current response was observed by the addition of various interference analytes (Figures 10a and 10b). Although glucose and fructose have the same molecular formula – so it may be expected that their response would be similar – they possess different chemical structures and functional groups, meaning that the electrochemical reactions are probably different on the CoS based sensor. Glucose has an aldehyde (-CHO) functional group, making it more active for the

oxidation process, leading to better selectivity compared to the other compounds that do not contain aldehydes.

Overall, CoS-ED exhibited a better selectivity as compared to CoS-HT. Table 2 shows a comparison of the activity of the present CoS sensor with earlier reported Co-based glucose sensors. It is observed that the CoS-ED electrode exhibited higher sensitivity compared to most of the other Co-based glucose sensors. However, the binary nanocomposite $\text{Co}(\text{OH})_2/\text{rGO}$ showed a higher sensitivity than the single material based CoS-ED sensors, attributed to the coupling of $\text{Co}(\text{OH})_2$ with reduced graphene oxide (rGO) and the use of a more conducting Au electrode substrate. Based on these results, it is concluded that CoS (especially the electrodeposited sample) can be employed as an efficient electrochemical sensor for the selective detection of glucose.

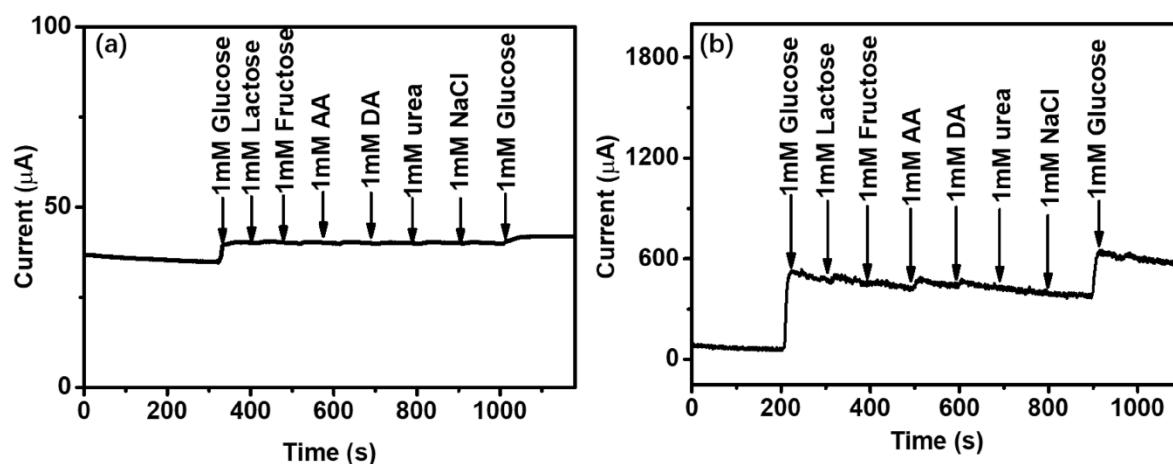


Figure 10. Selectivity test of (a) Co-HT and (b) CoS-ED based electrodes at a bias potential of 0.5 V with 1 mM glucose and different interferents such as lactose, fructose, ascorbic acid (AA), dopamine (DA), urea, NaCl in 100 mL of 0.1 M KOH with continuous stirring.

Table 2. Comparison of Co-based electrochemical sensors towards glucose.

Electrochemical sensor	Substrate	Electrolyte	Sensitivity ($\mu\text{A}/\text{mM}/\text{cm}^2$)	Ref.
Co_3O_4 Nanofibers	GC	0.1 M PBS	36.3	60
Co_3O_4 Nanoparticles	GC	PBS	13.5	61
CoO_x Nanostructures	GC	0.1 M PBS	163	62
$\text{Co}(\text{OH})_2/\text{rGO}$	Au	1 M NaOH	3320	63
Tremella-like CoS	GC	0.1 M NaOH	139	28
CoS-HT	FTO	0.1 M KOH	55.5	This work
CoS-ED	FTO	0.1 M KOH	330	This work

PBS: Phosphate buffered solution.

rGO: Reduced graphene oxide.

Conclusions

A systematic comparison of fabricated cobalt sulfide nanostructure (nanoflowers, nanosheets) based electrodes prepared by two different methods, hydrothermal and electrodeposition, for the dual applications towards OER and glucose detection has been undertaken. SEM images confirmed the growth of CoS in the morphology of nanoflowers and nanosheets *via* hydrothermal and electrodeposition methods, respectively. It was observed that the CoS-ED electrode demonstrated both enhanced OER performance and greater intrinsic activity compared to CoS-HT with a lower overpotential (~ 166 mV at 10 mAcm^{-2}), lower charge transfer resistance ($\sim 372 \Omega$), lower Tafel slope (86 mV dec^{-1}), and higher ECSA (\sim double that of CoS-HT). Moreover, the CoS-ED electrode-based sensor exhibited enhanced sensing activity, including higher sensitivity, better selectivity, and higher stability for electrochemical glucose detection compared to the CoS-HT electrode.

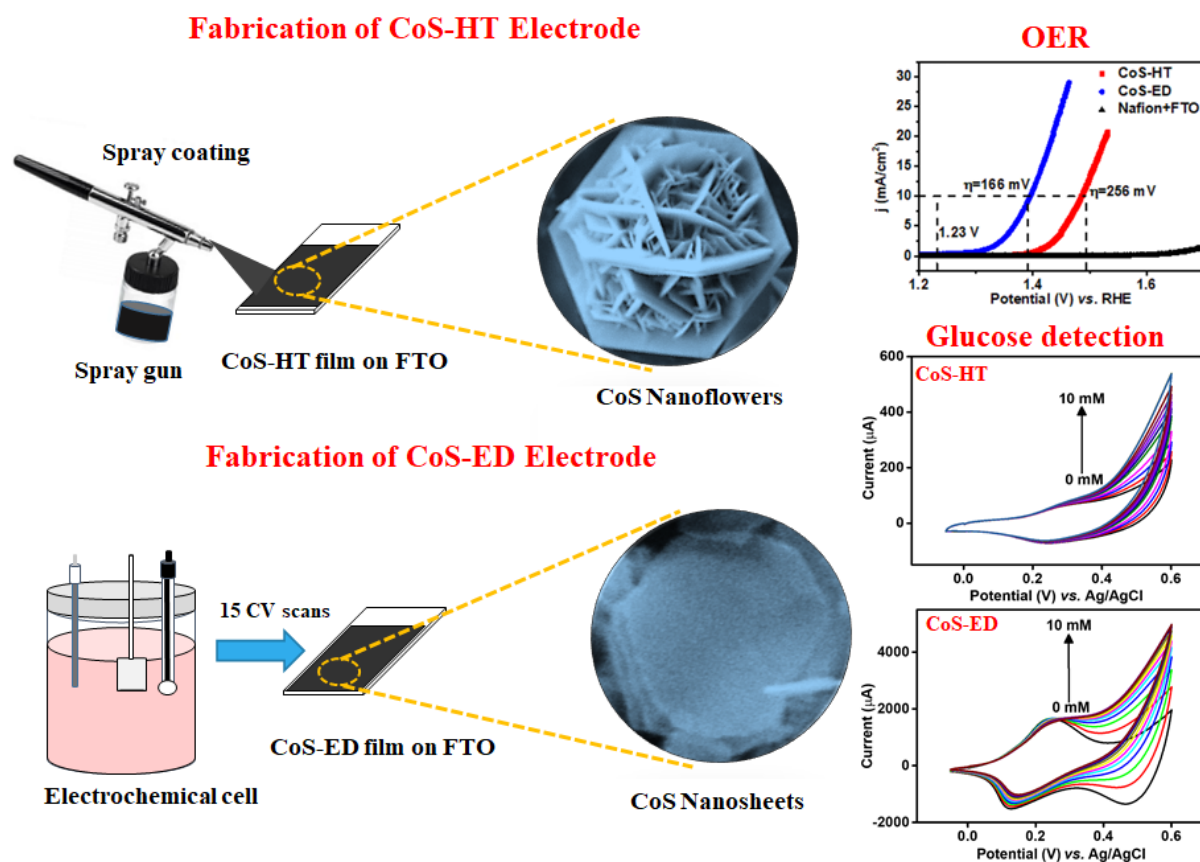
It is noted that the use of Nafion affects the performance of the CoS-HT film for both applications. The CoS-ED electrode demonstrated enhanced activity for the OER and glucose detection which is attributed to both (1) the use of a binder-free electrodeposition method and (2) approximately double the ECSA for the CoS-ED electrode, leading to the availability of more active sites and better intrinsic activity compared to the CoS-HT electrode. It can be concluded that the electrodeposited CoS material is a good choice in developing non-enzymatic glucose sensors for industrial purposes in the future. The present work opens up new avenues for the exploration and fabrication of other efficient and stable electrodes by the binder-free electrodeposition method for electrochemical water splitting and for electroanalytical applications.

Acknowledgements

D.S.S. would like to acknowledge the Australian Research Council (ARC) for funding through a Future Fellowship (FT170100315). X.Y.L is thankful to the China Scholarship Council for providing financial assistance through a PhD scholarship. The authors acknowledge the John

de Laeter Centre at Curtin University, and the use of equipment of the Curtin University Electron Microscope Facility, which is partially funded by the University, State and Commonwealth Governments of Australia.

TOC Graphic



The present work sheds light on the materials preparation methods for developing efficient, robust, and stable electrocatalyst systems for potential applications towards the OER, as well as for glucose detection.

References

1. G. F. Chen, T. Y. Ma, Z. Q. Liu, N. Li, Y. Z. Su, K. Davey, and S. Z. Qiao, *Adv. Funct. Mater.*, **26** (19), 3314-3323 (2016).
2. H. K. El Emam, S. I. El-Dek, and W. M. A. El Rouby, *J. Electrochem. Soc.*, **168** (5), (2021).
3. D. Feng, F. Wang, and Z. Chen, *Sens. Act. B*, **138** (2), 539-544 (2009).
4. P. K. Kannan and C. S. Rout, *Chemistry*, **21** (26), 9355-9359 (2015).
5. M. Marie, S. Mandal, and O. Manasreh, *Sensors*, **15** (8), 18714-18723 (2015).
6. P. Qu, Z. Gong, H. Cheng, W. Xiong, X. Wu, P. Pei, R. Zhao, Y. Zeng, and Z. Zhu, *RSC Advances*, **5** (129), 106661-106667 (2015).
7. J. Wang, D. F. Thomas, and A. Chen, *Anal. Chem.*, **80** (4), 997-1004 (2008).
8. B. You and Y. Sun, *Acc. Chem. Res.*, **51** (7), 1571-1580 (2018).
9. W. Wang, X. Xu, W. Zhou, and Z. Shao, *Adv. Sci.*, **4** (4), 1600371 (2017).
10. J. Hou, Y. Wu, B. Zhang, S. Cao, Z. Li, and L. Sun, *Adv. Funct. Mater.*, **29** (20), 1808367 (2019).
11. X. Wang, A. Vasileff, Y. Jiao, Y. Zheng, and S. Z. Qiao, *Adv. Mater.*, **31** (13), 1803625 (2019).
12. W.-J. Jiang, T. Tang, Y. Zhang, and J.-S. Hu, *Acc. Chem. Res.*, **53** (6), 1111-1123 (2020).
13. A. Heller and B. Feldman, *Chem. Rev.*, **108** (7), 2482-2505 (2008).
14. F. Wei, P. Patel, W. Liao, K. Chaudhry, L. Zhang, M. Arellano-Garcia, S. Hu, D. Elashoff, H. Zhou, and S. Shukla, *Clin. Cancer Res.*, **15** (13), 4446-4452 (2009).
15. A. Yu, Z. Liang, J. Cho, and F. Caruso, *Nano letters*, **3** (9), 1203-1207 (2003).
16. K. Beaver, A. Dantanarayana, and S. D. Minteer, *J Phys Chem B*, **125** (43), 11820-11834 (2021).
17. G. Huang, Z. Xiao, R. Chen, and S. Wang, *ACS Sustain. Chem. Eng.*, **6** (12), 15954-15969 (2018).
18. L. Chen, W. Ren, C. Xu, Q. Chen, Y. Chen, W. Wang, W. Xu, and Z. Hou, *J. Alloys Compd.*, 162038 (2021).
19. H. B. Tao, L. Fang, J. Chen, H. B. Yang, J. Gao, J. Miao, S. Chen, and B. Liu, *J. Am. Chem. Soc.*, **138** (31), 9978-9985 (2016).
20. A. P. Tiwari, Y. Yoon, T. G. Novak, A. Azam, M. Lee, S. S. Lee, G. h. Lee, D. J. Srolovitz, K. S. An, and S. Jeon, *Adv. Mater. Interfaces*, **6** (22), 1900948 (2019).
21. J. Wu, M. Liu, K. Chatterjee, K. P. Hackenberg, J. Shen, X. Zou, Y. Yan, J. Gu, Y. Yang, and J. Lou, *Adv. Mater. Interfaces*, **3** (9), 1500669 (2016).
22. H. Xu, H. Shang, L. Jin, C. Chen, C. Wang, and Y. Du, *J. Meter. Chem. A*, **7** (47), 26905-26910 (2019).
23. K. Prabakaran, M. Lokanathan, and B. Kakade, *Appl. Surf. Sci.*, **466** 830-836 (2019).
24. W. Li, D. Xiong, X. Gao, and L. Liu, *Chem. Commun.*, **55** (60), 8744-8763 (2019).
25. Y. Liu, N. Ran, R. Ge, J. Liu, W. Li, Y. Chen, L. Feng, and R. Che, *Chem. Eng. J.*, **425** 131642 (2021).
26. J. Xu, J. Li, D. Xiong, B. Zhang, Y. Liu, K.-H. Wu, I. Amorim, W. Li, and L. Liu, *Chem. Sci.*, **9** (14), 3470-3476 (2018).
27. U. Guth, W. Vonau, and J. Zosel, *Meas. Sci. Technol.*, **20** (4), 042002 (2009).

28. W. Wu, B. Yu, H. Wu, S. Wang, Q. Xia, and Y. Ding, *Mater. Sci. Eng. C Mater. Biol. Appl.*, **70** (Pt 1), 430-437 (2017).
29. S. Kong, Z. Jin, H. Liu, and Y. Wang, *J. Phys. Chem. C*, **118** (44), 25355-25364 (2014).
30. J.-Y. Lin and J.-H. Liao, *J. Electrochem. Soc.*, **159** (2), D65-D71 (2011).
31. J.-Y. Lin, J.-H. Liao, and S.-W. Chou, *Electrochim. Acta*, **56** (24), 8818-8826 (2011).
32. B. Qu, Y. Chen, M. Zhang, L. Hu, D. Lei, B. Lu, Q. Li, Y. Wang, L. Chen, and T. Wang, *Nanoscale*, **4** (24), 7810-7816 (2012).
33. J. Shi, X. Li, G. He, L. Zhang, and M. Li, *J. Mater. Chem. A*, **3** (41), 20619-20626 (2015).
34. B. Liu, S. Qu, Y. Kou, Z. Liu, X. Chen, Y. Wu, X. Han, Y. Deng, W. Hu, and C. Zhong, *ACS Appl. Mater. Interfaces*, **10** (36), 30433-30440 (2018).
35. T. Liu, Y. Liang, Q. Liu, X. Sun, Y. He, and A. M. Asiri, *Electrochem. Commun.*, **60** 92-96 (2015).
36. Y. Sun, C. Liu, D. C. Grauer, J. Yano, J. R. Long, P. Yang, and C. J. Chang, *J. Am. Chem. Soc.*, **135** (47), 17699-17702 (2013).
37. M. Sivakumar, M. Sakthivel, and S. M. Chen, *J. Colloid Interface Sci.*, **490** 719-726 (2017).
38. N. Jiang, L. Bogoev, M. Popova, S. Gul, J. Yano, and Y. Sun, *J. Mater. Chem. A*, **2** (45), 19407-19414 (2014).
39. A. Irshad and N. Munichandraiah, *ACS Appl Mater Interfaces*, **9** (23), 19746-19755 (2017).
40. M. R. Azhar, G. Hussain, M. O. Tade, D. S. Silvester, and S. Wang, *ACS Applied Nano Materials*, **3** (5), 4376-4385 (2020).
41. L. Durai and S. Badhulika, *New Journal of Chemistry*, **43** (30), 11994-12003 (2019).
42. W. Dong, X. Wang, B. Li, L. Wang, B. Chen, C. Li, X. Li, T. Zhang, and Z. Shi, *Dalton Trans.*, **40** (1), 243-248 (2011).
43. P. Guo, Y.-X. Wu, W.-M. Lau, H. Liu, and L.-M. Liu, *Journal of Alloys and Compounds*, **723** 772-778 (2017).
44. J. K. Yang, B. Liang, M. J. Zhao, Y. Gao, F. C. Zhang, and H. L. Zhao, *Sci. Rep.*, **5** 15001 (2015).
45. S. Sharma, D. Kumar, and N. Khare, *Polymer*, **231** (2021).
46. K. Guo, F. Shaik, J. Yang, X. Ren, and B. Jiang, *J. Electrochem. Soc.*, **168** (6), (2021).
47. H. Liang, A. N. Gandi, C. Xia, M. N. Hedhili, D. H. Anjum, U. Schwingenschlögl, and H. N. Alshareef, *ACS Energy Letters*, **2** (5), 1035-1042 (2017).
48. C. C. McCrory, S. Jung, I. M. Ferrer, S. M. Chatman, J. C. Peters, and T. F. Jaramillo, *J. Am. Chem. Soc.*, **137** (13), 4347-4357 (2015).
49. M. S. Faber, R. Dziejczak, M. A. Lukowski, N. S. Kaiser, Q. Ding, and S. Jin, *J. Am. Chem. Soc.*, **136** (28), 10053-10061 (2014).
50. S. Jin, *ACS Energy Letters*, **2** (8), 1937-1938 (2017).
51. U. K. Sultana and A. P. O'Mullane, *ChemElectroChem*, **6** (10), 2630-2637 (2019).
52. X. Xu, F. Song, and X. Hu, *Nat. Commun.*, **7** 12324 (2016).
53. S. Surendran, S. Shanmugapriya, H. Ramasamy, G. Janani, D. Kalpana, Y. S. Lee, U. Sim, and R. K. Selvan, *Applied Surface Science*, **494** 916-928 (2019).

54. Y. Li, X. Fu, W. Zhu, J. Gong, J. Sun, D. Zhang, and J. Wang, *Inorganic Chemistry Frontiers*, **6** (8), 2090-2095 (2019).
55. K. Li, X. Wang, S. Li, P. Urbankowski, J. Li, Y. Xu, and Y. Gogotsi, *Small*, **16** (4), e1906851 (2020).
56. J. P. John Wang, James Lim, and Bruce Dunn, *J. Phys. Chem. C*, **111** 14925-14931 (2007).
57. X. Cao, H. Yang, Q. Wei, Y. Yang, M. Liu, Q. Liu, and X. Zhang, *Inorg. Chem. Commun.*, **123** (2021).
58. S. Senthilkumar and R. Saraswathi, *Sens. Act. B*, **141** (1), 65-75 (2009).
59. M. Singh, U. Z. A. Ungku Faiz, S. Gravelins, Y. Suganuma, N. K. Kotoulas, M. Croxall, A. Khan-Trottier, C. Goh, and A.-A. Dhirani, *Nanoscale Advances*, **3** (13), 3816-3823 (2021).
60. Y. Ding, Y. Wang, L. Su, M. Bellagamba, H. Zhang, and Y. Lei, *Biosens. Bioelectron.*, **26** (2), 542-548 (2010).
61. C. Karuppiyah, S. Palanisamy, S.-M. Chen, V. Veeramani, and P. Periakaruppan, *Sens. Act. B*, **196** 450-456 (2014).
62. A. Salimi, R. Hallaj, and S. Soltanian, *Electroanalysis*, **21** (24), 2693-2700 (2009).
63. D. Jiang, Z. Chu, J. Peng, J. Luo, Y. Mao, P. Yang, and W. Jin, *Electrochim. Acta*, **270** 147-155 (2018).